

A New Method to Classify Type IIP/IIL Supernovae Based on their Spectra

XINGZHUO CHEN,¹ SHIHAO KOU,¹ AND XUEWEN LIU¹

¹*College of Physical Science and Technology,
Sichuan University, Chengdu, 610064,
People Republic of China*

(Received January 1, 0000; Revised January 1, 0000; Accepted January 1, 0000)

Submitted to ApJ

ABSTRACT

Type IIP and type IIL supernovae (SNe) are defined on their light curves, but the spectrum criteria in distinguishing these two type SNe remains unclear. We propose a new classification method. Firstly, we subtract the principal components of different wavelength bands in the spectra based on Functional Principal Components Analysis (FPCA) method. Then, we use Support Vector Machine (SVM) and Artificial Neural Network (ANN) to classify these two types of SNe. The best F1-Score of our classifier is 0.881, and we found that solely using H_α line at 6150-6800 Å for classification can reach a F1-Score up to 0.849. Our result indicates that the profile of the H_α is the key to distinguish the two type SNe.

Keywords: Supernova, Machine Learning

1. INTRODUCTION

Originated from massive stars ($8 \sim 20M_\odot$), Hydrogen Rich Core Collapse (CC) Supernovae (SNe) also known as type II SNe is one kind of SNe with conspicuous hydrogen spectral line at 6335 Å (Gal-Yam 2017). Some type II SNe are generally divided into 4 subtypes: IIP, IIL, I Ib and IIn. Moreover, some SNe with peculiar spectroscopic or light curve features are divided into type II-pec SNe, such as SN1987A (McCray 2017). Helium spectral lines at the wavelength 5876, 6678, 7065 Å are observable in type I Ib, while Type IIn spectra usually have a narrow H_α line at 6563 Å. As for Type IIP/IIL SNe, their definitions are based on the light curves.

The luminosity evolution of SNe are generally dominated by 4 mechanisms (Arcavi 2017): shock breakout, shock cooling & ejecta recombination, radioactive decay and circumstellar material (CSM) interaction. Type IIP SNe are characteristic of its plateau-like lightcurves, which fast rises to the peak (~ 15 days) after explosion and follows a plateau-phase (~ 90 days) which is powered from the cooling of ejecta. After the ‘plateau phase’ the magnitude will linearly decline (>1.4 Mag/100 day) with the propulsion of the nickel decay $^{56}\text{Ni} \rightarrow ^{56}\text{Co} \rightarrow ^{56}\text{Fe}$. In contrast, Type IIL SNe’ cooling phase is much shorter than Type IIP (typically less than 10 days) and its luminosity linearly decrease (~ 0.3 Mag/15day) (Gal-Yam 2017) after reaching maximum. Notably, Type I Ib SNe has the most various lightcurve and some of them even shows a double-peak light curves, the first of which is originated from the fast cooling effect after the explosion, while the second of which links to the high-energy photon escaping the relatively small-mass envelope (Arcavi 2017; Li *et al.* 2011; Richmond *et al.* 1994).

Many studies indicates the progenitor of Type IIP SNe is Red Super Giants (RSG) with mass range of 8.5-16.5 M_\odot (Smartt 2015), while Type I Ib SNe are generally originated from Yellow Super Giants (YSG) (Anderson *et al.* 2012). Moreover, some studies suggest Type IIn SNe’ progenitors are Luminous Blue Variables because the interaction between the core and Circumstellar Materials (CSM) (Schlegel 1990). Nonetheless, the progenitor of Type IIL SNe is on debate and only one observational evidence on SN2009kr suggests RSG or YSG could be progenitor (Elias-Rosa *et al.* 2011; Fraser *et al.* 2010).

In the former studies on Type IIP/IIL SNe, the absorption-emission ratio of H_α P-Cygni profile in Type IIL SNe is relatively smaller than Type IIP's, which is possibly because of Type IIP/IIL SNe's envelope mass and density gradient differences after the peak magnitude(Gutiérrez *et al.* 2014; Patat *et al.* 1994). Moreover, in a study on H_α and O(I)7774 equivalent width(EW), the spectra of Type IIP SNe have a smaller ratio $EW_{O17774}/EW_{H_\alpha}$ (Faran *et al.* 2014a). Additionally, at the peak luminosity, Type IIL SNe' absolute magnitude is -17.44 ± 0.22 while Type IIP' is -15.66 ± 0.16 (Li *et al.* 2011). However, unlike the classification in Type I SNe(Sun & Gal-Yam 2017), scant spectroscopic criteria are presented to determine Type IIP/IIL SNe.

Recently, with the advance of machine-learning algorithm and applications, new spectroscopic and photometric classification methods are introduced. Several studies have been conducted in photometric classification and instant detection of SNe and other transients via machine learning algorithms(du Buisson *et al.* 2015; Bloom *et al.* 2012; Richards *et al.* 2012). With Principal Component Analysis (PCA) and Functional Principal Analysis (FPCA) algorithm, the light curves of SNe are able to described into fewer parameters(Rubin & Gal-Yam 2016; He *et al.* 2018). Furthermore, combining PCA with other machine learning algorithms, i.e. Self Organizing Maps and K-means, the spectral features in different subtypes of Type Ia SNe has been studied(Sasdelli *et al.* 2016).

In this study, we applied Functional Principal Component Analysis (FPCA) on the different wave bands of Type IIP/IIL SNe' spectra, then use Support Vector Machine (SVM) and Artificial Neural Network (ANN) to classify the types of SNe from the principal components (FPCA scores). In § 2, we will introduce the data source and the algorithms (FPCA, SVM and ANN) used in the paper. In § 3, we will discuss the performance of our classifiers. The prospective and the summary will be presented in § 4. All the codes used in the analysis are uploaded onto <https://github.com/GeronimoChen/IIL-IIP-SNe>.

2. METHOD

2.1. Pre-processing the data

All the spectra of Type II SNe (/IIP/IIL/Iib/IIn) are downloaded from WISEREP(Yaron & Gal-Yam 2012) for our analysis. Because there are only Type IIL in the database, we tried to find 6 more Type IIL SNe from other literatures to expand the dataset, which is shown in Table.2.1. As the unclassified Type IIL has been concluded, the dispersion of different types' SNe object and spectra are shown in Fig.1.

Table 1. More Type IIL SNe from Other Literature

Supernovae Name	Number of Spectra	Type in WISEREP	Reference
SN1980K	6	II	(Eldridge & Tout 2004)
SN1979C	4	II	(Ray <i>et al.</i> 2001)
SN2013hj	5	II	(Bose <i>et al.</i> 2016)
SN2013by	18	II	(Valenti <i>et al.</i> 2015)
SN2013ej	112	II	(Yuan <i>et al.</i> 2016)
SN2009kr	2	IIn	(Anderson <i>et al.</i> 2012)

The pre-processing of the spectra are discussed in the Section 5, which is constitute of removing redshifts, Savitz-Golay filter(Savitzky & Golay 1964), removing continuum spectra. Then, the as-prepared spectra are divided into 9 small wavelength windows and 2 long wavelength windows, as is shown in Fig.2. Referring to peer literatures(Singh *et al.* 2018; Smith *et al.* 2010; Taddia *et al.* 2016; Gutiérrez *et al.* 2018; Anderson *et al.* 2018; de Jaeger *et al.* 2018; Marcaide *et al.* 2002; Maguire *et al.* 2010), we have concluded the major spectral lines in SN identification into the Table 1. Because of the conspicuous hydrogen line in most Type II SNe, we carefully selected the H_α and H_β wave-windows to include all the absorption and emission parts for most spectra. Most the small wave-windows are denoted with the spectral lines in the spectra, except the wave-window 'Gap', which was excluded initially due to the H_2O spectral line at 7165 Å. However, some Type II SNe may embody calcium spectral line (Ca(II)7291,7323) in this reagon(de Jaeger *et al.* 2018; Maguire *et al.* 2010; Faran *et al.* 2014a), so this wavelength window is preserved. Furthermore, wavelength at 6800-7000 and 7400-7700 Å are excluded from the small wavelength windows due to the

Table 2. Wave-Window Ranges and Spectral Lines

Name	Wavelength Range (Å)	Elements and Spectral Lines	Available Type IIL/IIP spectra
FeMg	4200-4600	H_γ 4340, H_δ 4102, Ba(II)4554	170/667
H_β	4600-4900	H_β 4861	181/717
FeOMgSi	4900-5250	Fe(II)4924,5018,5108,5169. O(III)4959,5007.	176/733
S	5250-5800	S(II)5454,5433. O(V)5597.	154/700
Na	5800-6150	Na(I)5876,5896. He(I)5876. Ba(II)6142.	168/722
H_α	6150-6800	H_α 6563. He(I)6678, O(I)6300,6364. N(II)6548. Sc(II)6247	177/735
Gap	7000-7400	Fe(II)7155. He(I)7065. O(II)7319,7330. Ca(II)7291,7323	159/672
NaMg	7700-8200	Na(I)8183,8195	111/491
Ca	8200-8900	Ca(II)8498,8542,8662. O(I)7774.	113/440
Visible	4000-7000	/	115/567
Expand	4000-9000	/	63/306

NOTE—The names of each wave-window are roughly selected based on the spectral line given in WISEREP, but not all the elements exhibit in Type II SNe.

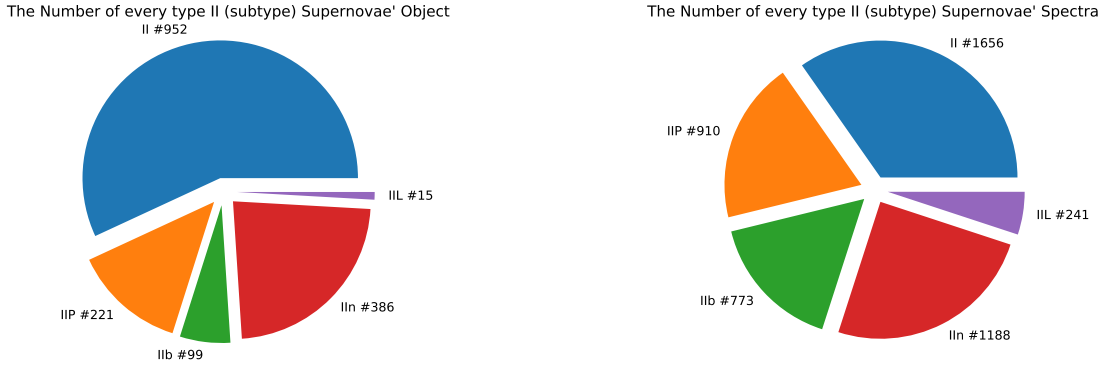


Figure 1. The pie chart of Type II/IIP/IIL/IIb/IIn objects and spectra. The number of objects/data are marked with the type.

telluric spectral line (O_2 6867, 7620). Relating to a study in PCA analysis in Type Ia spectra (Sasdeli *et al.* 2016), we kept two long wave-windows here, which are the ‘visible’ wavelength at 4000-7000 Å and ‘expand’ wavelength at 4000-9000 Å. Because of the equipments limitation and redshift effect, some wave-windows are not fully sampled or even not sampled in a spectrum, which cause an extra data loss in the following training for the classifying algorithm. The number available spectra in each wave-windows are also counted in Table 1.

2.2. FPCA algorithm

We use Functional Principal Components Analysis (FPCA) for the first process of each wave-window in order to acquire a series principal scores of each spectrum. This algorithm was applied to SNe’ light curve analysis before (He *et al.* 2018).

The FPCA algorithm aims to give a set of orthonormal functions, which could represent a series of trajectory via their linear combination (Hall *et al.* 2006; Jones & Rice 1992; Peng & Paul 2007). Considering n SNe spectra, $X_n(\lambda)$, which could be represented in the following equations:

$$X_n(\lambda) = \mu(\lambda) + \sum_{m=1}^{\infty} \beta_{m,n} \phi_m(\lambda) \quad (1)$$

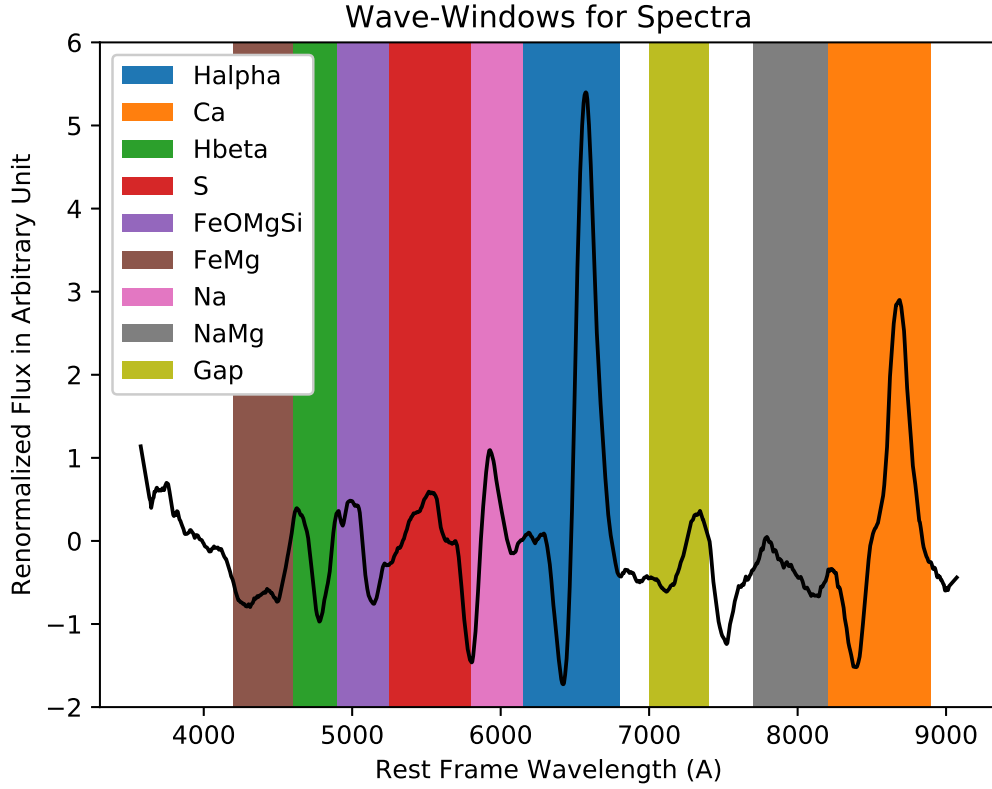


Figure 2. The wave-windows chosen for analysis. The range and the element spectra composition are listed in Table 1.

Where β_m is the m -th FPCS scores, $\phi_m(\lambda)$ is the m -th basis functions and $\mu(\lambda)$ is the average spectrum of all selected spectra. Because the mean function has been subtracted into $\mu(\lambda)$, the average of each order FPCS scores for all spectra are zero. Every basis functions preserves orthonormal conditions, and the order of basis functions are sorted by the variance of FPCS scores:

$$\int_{\lambda_{min}}^{\lambda_{max}} \phi_j(\lambda)\phi_k(\lambda)d\lambda = \delta_{jk} \quad (2)$$

$$\forall m : Var(\beta_{m,n=1,2,\dots,n_{max}}) > Var(\beta_{m+1,n=1,2,\dots,n_{max}}) \quad (3)$$

As every basis functions are orthonormal, the m -th FPCS score of a single spectrum can be calculated via convolution in the selected wave-window $\lambda_{min} \sim \lambda_{max}$:

$$\beta_{m,n} = \int_{\lambda_{min}}^{\lambda_{max}} \phi_m(\lambda) (X_n(\lambda) - \mu(\lambda)) d\lambda \quad (4)$$

In order to preserve the most information of spectra $X(\lambda)$, the FPCS scores of each order should as space as possible (the variance is as big as possible), and the selection of basis functions obeys the following equation.

$$\phi_n(\lambda) = argmax \left(Var \left(\int_{\lambda_{min}}^{\lambda_{max}} (X(\lambda) - \mu(\lambda)) \phi_n(\lambda) d\lambda \right) \right) \quad (5)$$

In this literature, we adopt `fPCA` package in R language (Peng & Paul 2007) for FPCA analysis, which use a gradient optimize method to acquire the best set of basis functions. With the order of basis function increases, the FPCS scores are converge to zero, which gives possible to set a highest order and perserves most informations in the raw spectra $X_n(\lambda)$.

We solved 30 basis functions for each small wave-windows Table 1. As for the large wave-windows, 50 basis functions are solved in ‘Visible’ wave-window and 40 basis functions are solved in ‘Expand’ wave-window. We select some basis functions and average functions shown in Fig.3. Also, we managed to re-construct some spectra for the comparison with the original data, which is shown in Section 6

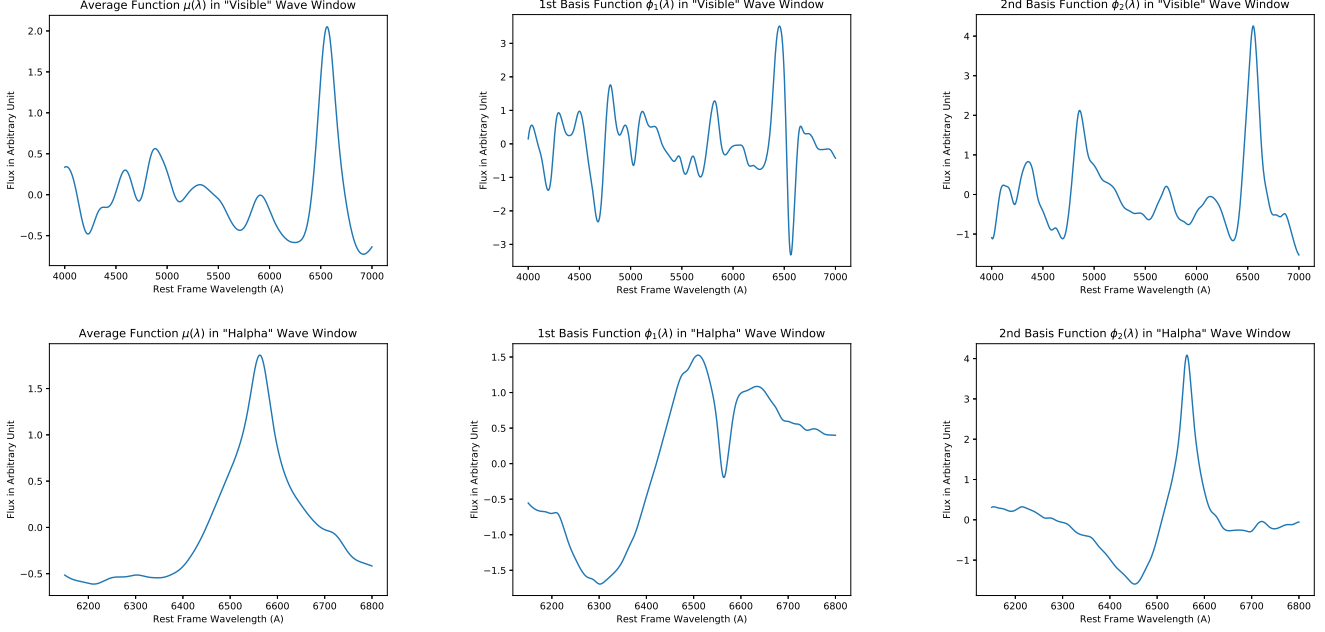


Figure 3. Average Function, 1st and 2nd basis function in ‘Visible’ and ‘ $H\alpha$ ’ wave-windows.

2.3. Support Vector Machine

From the as-discussed FPCA algorithm, all the spectra can be represented with a series of FPCA scores. Although some tendencies of different type SNe can be observed in some selected dimensions of FPCA scores’ parametric space Section 7, we firstly choose Support Vector Machine (SVM)(Chen *et al.* 2005; Chang & Lin 2011; Cristianini & Ricci 2008) for the classification of Type IIL/IIP SNe.

SVM is a popular machine learning method for classification which aims to find the optimal hyperplane to separate two sets of dots with largest margin distance, as is shown in Fig.4. This method is firstly proposed in 1992(Boser *et al.* 1992)

Consider two kinds of nodes in a hyperspace, the target of SVM is to find a hyperplane which could separate the data, which is written in the form:

$$0 = X \cdot \omega + b \quad (6)$$

Where X is the coordination on the hyperplane, ω is the weight of each dimension and b is the biase. The dots which are closest to the hyperplane are denoted as support vectors, the distance between the support vector and the hyperplane is:

$$Min_i \left(\frac{\omega \cdot X_i + b}{\|\omega\|} \right) \quad (7)$$

Where X_i is the coordination of the nodes. The minimal is reached if the X_i is the support vector. To construct an optimize hyperplane, the distances between the support vectors and the hyperplane should be as large as possible, the optimization target:

$$Max_{\omega, b} \left[Min_i \left(\frac{\omega \cdot X_i + b}{\|\omega\|} \right) \right] \quad (8)$$

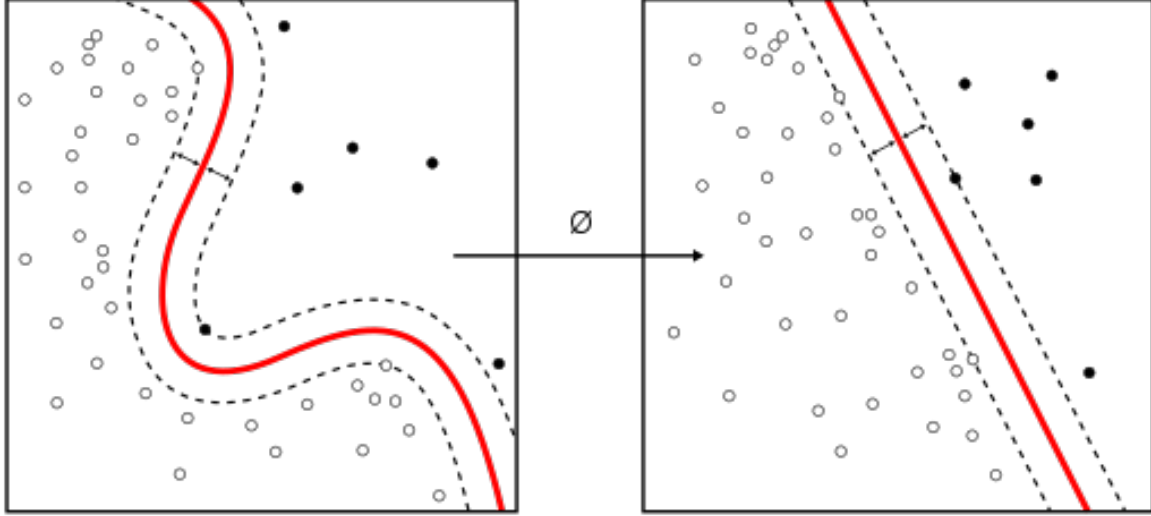


Figure 4. An illustrative picture of SVM, By Alisneaky, svg version by User:Zirguez <https://commons.wikimedia.org/w/index.php?curid=47868867>

If the distance between the support vector and the hyperplane is denoted to 1, then the optimization target is:

$$\text{Max}\left(\frac{1}{\|\omega\|}\right), \text{ subject to : } y_i(\omega \cdot X_i + b) > 1 \quad (9)$$

Where $y_i = \pm 1$ is the sign of the nodes, which marks their tags (IIP or IIL). Considering the intrinsically not separable nodes, a slack variable is introduced to gauge the misclassification:

$$1 - \xi_i = y_i(\omega \cdot X_i + b), \quad \xi_i \geq 0 \quad (10)$$

The cost function for the optimization is written as below:

$$L(\omega, b, \xi) = \frac{1}{2}\|\omega\|^2 + C \sum_i \xi_i \quad (11)$$

In this paper, we use `python.sklern.svm` for SVM classification, radial basis function (RBF) is used for non-linear classification, the kernel function and the distance are written as:

$$K(x, x') = \exp\left(-\gamma \frac{\|x - x'\|^2}{\sigma^2}\right) \quad (12)$$

$$K(\omega, X) + b = \exp\left(-\gamma \frac{\|x - x'\|^2}{\sigma^2}\right) + b \quad (13)$$

If no further explanation are given, we set the default parameters $C = 3020$ and γ automatically generated by the machine, which promises the best performance of SVM algorithm in most classifications in this literature.

2.4. Artificial Neural Network

A simple Artificial Neural Network (ANN) is composed of three parts: input layer, hidden layers and the output layer (LeCun *et al.* 2015). Nodes in adjacent layers are linked with different weights. In the ANN, data are propagated from the input layer to the output layer with the equation:

$$z_i = \omega_i \cdot y_i + b_{y_{i+1}} = f_{i+1}(z_i) \quad (14)$$

Where ω_i is the weight, b is the bias and $f_{i+1}(z_i)$ is the activation function of nodes in each layer. The output layer will give the probabilistic classification upon a certain input data. In this paper, we use rectified linear unit

($f(z) = \max(0, z)$) as the hidden layer's activation function, and sigmoid function ($f(z) = 1/(1 + \exp(-x))$) as the output layer's activation function.

The weight and bias parameters are trained using backpropogation procedure. In this paper, we choose binary cross entropy(Shannon 2001) as the loss function, which is written as:

$$L(y_r, y_p) = - \sum_i [y_r \ln(y_p) + (1 - y_r) \ln(1 - y_p)] \quad (15)$$

Where y_r is the true probability 0 or 1, y_p is the probability given by the neural network. For each training epoch, the upload of weight and biase are uploaded upon the gradient of the loss function, $g_\omega = \frac{\partial L}{\partial \omega}$, $g_b = \frac{\partial L}{\partial b}$. In this paper, we use Adam algorithm(Kingma & Ba 2014) for optimization, from which the weights and biase are updated with:

$$m_t = \beta_1 m_{t-1} + (1 - \beta_1) g \quad (16)$$

$$v_t = \beta_2 v_{t-1} + (1 - \beta_2) g \quad (17)$$

$$\hat{m}_t = m_t / (1 + \beta_1^t) \quad (18)$$

$$\hat{v}_t = v_t / (1 + \beta_2^t) \quad (19)$$

$$\theta_{new} = \theta_{old} - \alpha \hat{m}_t / (\sqrt{\hat{v}_t} + \epsilon) \quad (20)$$

Where θ is weight or biase, m_t and v_t are the t-th epoch first and second momentum, $\epsilon = 10^{-8}$ is set to avoid overfull. We use the default decay parameters $\beta_1 = 0.9$, $\beta_2 = 0.999$ and the learning rate $\alpha = 0.001$.

In this paper, we use the integrated deep learning package `python.keras` for ANN training and testing. Regulizations are not introduced considering they cannot increase the performance in this paper.

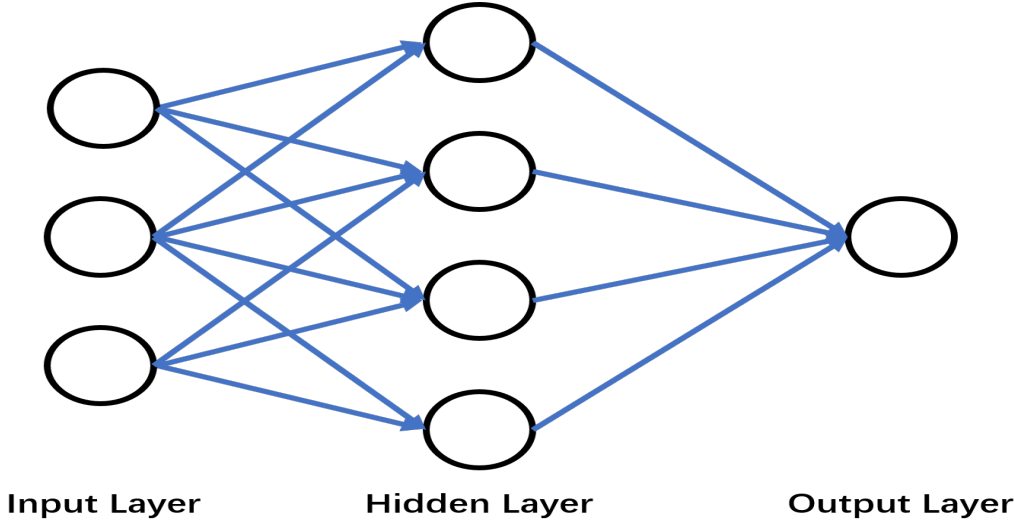


Figure 5. The Formation of Artificial Neural Network. Here, only one neurone is used in output layer for dichotomy classificatin of Type IIP/IIL SNe.

2.5. Performance evaluation

In each training and testing process, we randomly discard some Type IIP SNe at the outset, in order to keep a same number of Type IIP/IIL spectra in our dataset. Secondly, the dataset is splited into training set and testing set, which contains 80% and 20% of the data. When the classifier has trained on the training set, we use F1-Score to evaluate the performances of our classifiers. the definition of F1-Score is as follows(Olson & Delen 2008):

$$\text{Precision} = \frac{\text{TruePositive}}{\text{TruePositive} + \text{FalsePositive}} \quad (21)$$

$$\text{Recall} = \frac{\text{TruePositive}}{\text{TruePositive} + \text{FalseNegative}} \quad (22)$$

$$\text{F1 - Score} = \frac{2}{\frac{1}{\text{Precision}} + \frac{1}{\text{Recall}}} \quad (23)$$

Where true positive is the number of ‘positive’ spectra retrived by the classifier, true negative is the number of ‘negative’ spectra that didn’t retrived by the classifier, false positive is the number of ‘negative’ wrongly retrived by the classivier and false negative is the number of ‘positive’ spectra didn’t retrived by the classifier. We calculated the precision, recall and F1-Score of Type IIP and Type IIL seperately, then adopt the average of two types.

Because the number of Type IIL/IIP spectra are too small and biased, as is shown in Table 1, we adopt a cross validation method to evaluate our classifiers’ performance. The training- and testing-process will repeat several times and the dataset are re-splitted before each training process. Finally, we calculate the average precision, recall and F1-Score to evaluate the classifier. In addition, the standard error of precision, recall and F1-Score are also calculated in order to evaluate the stability of classifiers.

3. RESULTS AND DISCUSSION

3.1. *The Performance of Classifiers in One Wave-Window*

We firstly test the performance of SVM using only one wave-window and calculate the F1-Score, the results are shown in Table 9. In this trial, only first 30 FPCA scores of the ‘Visible’ and ‘Expand’ are selected, to perform an unbiased test to compare the performance of smaller and larger wave-windows. We notice that both ‘Visible’ and ‘Expand’ wavw-windows have a relatively high F1-Score, which reaches to 0.815 and 0.83. In contrast, the ‘NaMg’ wave-window’s F1-Score is the lowest among others. Moreover, we notice the F1-Score of ‘ H_α ’ window reaches 0.809, which is the third highest among 11.

Additionally, we utilized several ANN models for the classification using 30 FPCA scores in one wave-window, the results of which is shown in Table 6. A simple three-layered neural network is constructed in `python.keras` framework, the parameters are listed in Table 3.1. In the list of classification results Table 6, only the scores of best-performed model are shown in the table. The F1-Score of ANN is higher than SVM’s in all wave-windows. Notably, the F1-Score of ‘ H_α ’ wave-window, which reaches 0.849, is the highest among other 8 small wave-windows.

Although large wave-windows are not excel at re-constructing every details of a spectrum Section 5, its performance is higher than small wave-windows, we suggest this phenomenon is caused by the normalization process in pro-processing the spectra. For the precision in solving FPCA basis functions, every wave-windows are normalized seperately. As a consequence, the flux ratio between each small wave-windows are omitted. Considering this part of information is directly linked to the element ratios in SNe, it is persumable to obtain a worse result when solely small wave-windows are utilized. In contrast, a comprehensive wave-window contains multiple spectral lines, and the information about the element ratios are preserved, which promises a better performance.

Table 3. ANN parameters for one-window classification

Items	Keys
Input Layer	30
Hidden Layer	See the Table 6
Activition Function	ReLU
Output Layer	1
Activition Function	sigmoid
Optimisztion Method	AdamBoost
Regularization	None

3.2. *Performance with More Basis Functions*

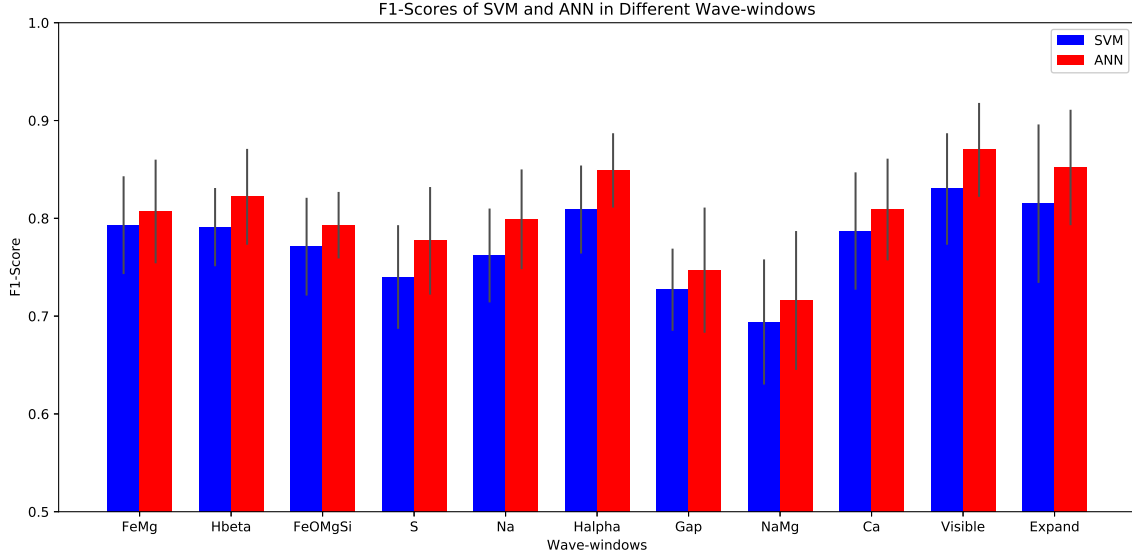


Figure 6. The F1-Score in SVM and ANN of every wave-windows. Error bars are plotted in the picture. The F1-Score of ANN are generally higher than SVM's. Data from Table 6, Table 9

With more basis functions, it is possible to re-construct the spectra with a higher fidelity, albeit more computational costs in solving basis functions. However, whether more FPCA scores will increase the accuracy in classification remains a question. In this section, we tried to change the number of basis functions in FPCA analysis, and discuss the minimal number of basis functions for the classification. Relating to the F1-Scores in Section 3.1, we choose the best small wave-window and the best large wave-window, ' H_α ' and 'Visible' for the following discussion. The models of ANN are the same in Section 3.1 We plotted our results into Fig.7, the relating data are shown in Section 2.1. In ' H_α ' wave-window, F1-Score reaches 0.839 when 10 basis functions are utilized, while the F1-Score in 'Visible' wave-window for 10 basis functions is 0.842. If the dimension is larger than 10, the F1-Scores of two wave-windows are more than 90% of the wave-windows' best F1-Score, while the outcome slopes when the dimension is smaller than 10. Moreover, we can observe fluctuations in 'Visible' bands, indicating the instability of the ANN model in the chosen wave-window, which is also confirmed by the relatively large variation (0.5 – 0.9) of F1-Score. Accordingly, we suggest 10 basis functions is adequate for the classification of Type IIP/IIL SNe.

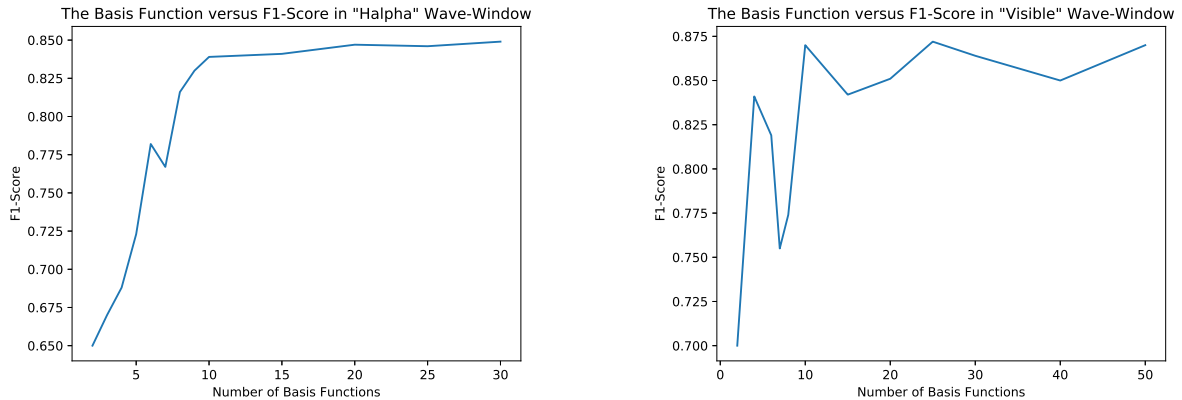


Figure 7. The relation between the FPCA scores dimension and the F1-Score in ' H_α ' and 'Visible' wave-windows.

Moreover, we availed the most data and attempt to test the stratosphere. We tested the classifiers' performance in using 9 small wave-windows or all 11 wave-windows, the total number of FPCA scores of which reaches 270 and 360. So, the input dimension is 270 or 360. Using the default parameters in SVM $C = 3020$ still performs well. However,

Table 4. The Best-Performed Classifiers

Classifier	Number of Wave-Windows	Hidden-Layer Nodes	Precision	Recall	F1-Score	σ_P	σ_R	σ_F
SVM	9	/	0.829	0.831	0.824	0.071	0.071	0.074
SVM	11	/	0.831	0.829	0.824	0.078	0.079	0.080
ANN	9	90	0.856	0.858	0.852	0.053	0.054	0.056
ANN	11	30	0.886	0.886	0.881	0.054	0.059	0.057

NOTE—In this scenario, the parameter for SVM C=3020.

we found that using neural-network with 90 or 30 nodes in the hidden layer performs the best. The results are listed below.

Comparing to the SVM in one wave-window Table 9, the results in using multiple wave-windows did not increase whatsoever, probably because the higher dimension of features infects SVM’s performance (Chou & Ko 2017; Nakayama *et al.* 2017). In using ANN for classification, we found the F1-Score reaches 0.881, which is the best among other classification methods in this paper.

4. SUMMARY

We decomposed Type II SNe spectra into different basis functions via FPCA algorithm. Based on the FPCA scores of every spectra, we have trained SVM and ANN to classify Type IIP and IIL SNe, two types of which has scant spectroscopic discrepancies. The spectra are divided into 9 small-size wave-windows and 2 large-size wave-windows for FPCA analysis respectively. The best F1-Score we got is 0.881. It is, for the first time, the effectively spectroscopic classification of Type IIP/IIL SNe.

Using the FPCA algorithm in different wave-windows, we successfully compressed the data of some certain spectral lines into 30-50 FPCA scores with minimal data loss. This processing trick do not only preserves the most informations about the elements explosion speed, but also enables us to apply some simple machine-learning models for classifications.

Moreover, we notice that only using a small-scale wave window at 6150-6800 Å, which covers the P Cygni profile of H_α line, outperforms to other spectral features in classification with its F1-Score up to 0.849, probable because of the higher signal-to-noise ratio. We suggest FPCA analysis directly on spectral line of a specific element could be a new approach in SNe classification analysis.

In the future, we will investigate the relationship between the basis functions (the principal components in spectra) and the explosion profile of SNe to expand the classification method on Type I SNe. Moreover, we will integrate other informations, such as temperature and the color evolution of SNe into the model for a higher accuracy.

Xingzhuo Chen thanks to Prof. Avishay Gal-Yam (Weizmann Institute of Science) and Prof. Lifan Wang (Purple Mountain Observatory) for supportive discussion. We thanks Weizmann Interactive Supernova data REPOSITORY (WISeREP) <https://wiserep.weizmann.ac.il/> and Transient Name Server (TNS) <https://wis-tns.weizmann.ac.il/> for the data.

Software: python,keras,scikit-learn,R-fpca(Peng & Paul 2007)

REFERENCES

- Anderson, J. P., Habergham, S. M., James, P. A., & Hamuy, M. 2012. Progenitor mass constraints for core-collapse supernovae from correlations with host galaxy star formation. *MNRAS*, **424**(Aug.), 1372–1391.
- Anderson, J. P., Dessart, L., Gutiérrez, C. P., Krühler, T., Galbany, L., Jerkstrand, A., Smartt, S. J., Contreras, C., Morrell, N., Phillips, M. M., Stritzinger, M. D., Hsiao, E. Y., González-Gaitán, S., Agiozzo, C., Castellón, S., Chambers, K. C., Chen, T.-W., Flewelling, H., Gonzalez, C., Hosseinzadeh, G., Huber, M., Fraser, M., Inserra, C., Kankare, E., Mattila, S., Magnier, E., Maguire, K., Lowe, T. B., Sollerman, J., Sullivan, M., Young, D. R., & Valenti, S. 2018. The lowest-metallicity type II supernova from the highest-mass red supergiant progenitor. *Nature Astronomy*, **2**(July), 574–579.

- Arcavi, I. 2017. *Hydrogen-Rich Core-Collapse Supernovae*. Page 239.
- Bloom, J. S., Richards, J. W., Nugent, P. E., Quimby, R. M., Kasliwal, M. M., Starr, D. L., Poznanski, D., Ofek, E. O., Cenko, S. B., Butler, N. R., Kulkarni, S. R., Gal-Yam, A., & Law, N. 2012. Automating Discovery and Classification of Transients and Variable Stars in the Synoptic Survey Era. *PASP*, **124**(Nov.), 1175.
- Bose, S., Kumar, B., Misra, K., Matsumoto, K., Kumar, B., Singh, M., Fukushima, D., & Kawabata, M. 2016. Photometric and polarimetric observations of fast declining Type II supernovae 2013hj and 2014G. *MNRAS*, **455**(Jan.), 2712–2730.
- Boser, Bernhard E., Guyon, Isabelle M., & Vapnik, Vladimir N. 1992. A Training Algorithm for Optimal Margin Classifiers. *Pages 144–152 of: Proceedings of the Fifth Annual Workshop on Computational Learning Theory*. COLT '92. New York, NY, USA: ACM.
- Chang, Chih-Chung, & Lin, Chih-Jen. 2011. LIBSVM: A Library for Support Vector Machines. *ACM Trans. Intell. Syst. Technol.*, **2**(3), 27:1–27:27.
- Chen, P-H., Lin, C-J., & Schölkopf, B. 2005. A tutorial on v-support vector machines. *Applied Stochastic Models in Business and Industry*, **21**(2), 111–136.
- Chou, E. P., & Ko, T.-W. 2017. Dimension Reduction of High-Dimensional Datasets Based on Stepwise SVM. *ArXiv e-prints*, Nov.
- Cristianini, Nello, & Ricci, Elisa. 2008. Support Vector Machines. *In: Encyclopedia of Algorithms*.
- de Jaeger, T., Galbany, L., Gutiérrez, C. P., Filippenko, A. V., Zheng, W., Brink, T. G., Foley, R. J., Sánchez, S. F., Channa, S., de Kouchkovsky, M., Halevi, G., Kilpatrick, C. D., Kumar, S., Molloy, J., Pan, Y.-C., Ross, T. W., Shivvers, I., Siebert, M. R., Stahl, B., Stegman, S., & Yunus, S. 2018. SN 2016esw: a luminous Type II supernova observed within the first day after the explosion. *MNRAS*, **478**(Aug.), 3776–3792.
- du Buisson, L., Sivanandam, N., Bassett, B. A., & Smith, M. 2015. Machine learning classification of SDSS transient survey images. *MNRAS*, **454**(Dec.), 2026–2038.
- Eldridge, J. J., & Tout, C. A. 2004. Exploring the divisions and overlap between AGB and super-AGB stars and supernovae. *Mem. Soc. Astron. Italiana*, **75**, 694.
- Elias-Rosa, N., Van Dyk, S. D., Li, W., Silverman, J. M., Foley, R. J., Ganeshalingam, M., Mauerhan, J. C., Kankare, E., Jha, S., Filippenko, A. V., Beckman, J. E., Berger, E., Cuillandre, J.-C., & Smith, N. 2011. The Massive Progenitor of the Possible Type II-Linear Supernova 2009hd in Messier 66. *ApJ*, **742**(Nov.), 6.
- Faran, T., Poznanski, D., Filippenko, A. V., Chornock, R., Foley, R. J., Ganeshalingam, M., Leonard, D. C., Li, W., Modjaz, M., Serduke, F. J. D., & Silverman, J. M. 2014a. A sample of Type II-L supernovae. *MNRAS*, **445**(Nov.), 554–569.
- Faran, T., Poznanski, D., Filippenko, A. V., Chornock, R., Foley, R. J., Ganeshalingam, M., Leonard, D. C., Li, W., Modjaz, M., Nakar, E., Serduke, F. J. D., & Silverman, J. M. 2014b. Photometric and spectroscopic properties of Type II-P supernovae. *MNRAS*, **442**(July), 844–861.
- Faran, T., Nakar, E., & Poznanski, D. 2018. The evolution of temperature and bolometric luminosity in Type II supernovae. *MNRAS*, **473**(Jan.), 513–537.
- Fraser, M., Takáts, K., Pastorello, A., Smartt, S. J., Mattila, S., Botticella, M.-T., Valenti, S., Ergon, M., Sollerman, J., Arcavi, I., Benetti, S., Bufano, F., Crockett, R. M., Danziger, I. J., Gal-Yam, A., Maund, J. R., Taubenberger, S., & Turatto, M. 2010. On the Progenitor and Early Evolution of the Type II Supernova 2009kr. *ApJL*, **714**(May), L280–L284.
- Gal-Yam, A. 2017. *Observational and Physical Classification of Supernovae*. Page 195.
- Gutiérrez, C. P., Anderson, J. P., Hamuy, M., González-Gaitán, S., Folatelli, G., Morrell, N. I., Stritzinger, M. D., Phillips, M. M., McCarthy, P., Suntzeff, N. B., & Thomas-Osip, J. 2014. H Spectral Diversity of Type II Supernovae: Correlations with Photometric Properties. *ApJL*, **786**(May), L15.
- Gutiérrez, C. P., Anderson, J. P., Sullivan, M., Dessart, L., González-Gaitán, S., Galbany, L., Dimitriadis, G., Arcavi, I., Bufano, F., Chen, T.-W., Dennefeld, M., Gromadzki, M., Haislip, J. B., Hosseinzadeh, G., Howell, D. A., Inserra, C., Kankare, E., Leloudas, G., Maguire, K., McCully, C., Morrell, N., Olivares E, F., Pignata, G., Reichart, D. E., Reynolds, T., Smartt, S. J., Sollerman, J., Taddia, F., Takáts, K., Terreran, G., Valenti, S., & Young, D. R. 2018. Type II supernovae in low-luminosity host galaxies. *MNRAS*, **479**(Sept.), 3232–3253.
- Hall, P., Müller, H.-G., & Wang, J.-L. 2006. Properties of principal component methods for functional and longitudinal data analysis. *ArXiv Mathematics e-prints*, Aug.
- He, S., Wang, L., & Huang, J. Z. 2018. Characterization of Type Ia Supernova Light Curves Using Principal Component Analysis of Sparse Functional Data. *ApJ*, **857**(Apr.), 110.
- Hogg, D. W., Baldry, I. K., Blanton, M. R., & Eisenstein, D. J. 2002. The K correction. *ArXiv Astrophysics e-prints*, Oct.

- Jones, M. C., & Rice, John A. 1992. Displaying the Important Features of Large Collections of Similar Curves. *The American Statistician*, **46**(2), 140–145.
- Kingma, D. P., & Ba, J. 2014. Adam: A Method for Stochastic Optimization. *ArXiv e-prints*, Dec.
- LeCun, Yann, Bengio, Yoshua, & Hinton, Geoffrey E. 2015. Deep learning. *Nature*, **521**(7553), 436–444.
- Li, W., Leaman, J., Chornock, R., Filippenko, A. V., Poznanski, D., Ganeshalingam, M., Wang, X., Modjaz, M., Jha, S., Foley, R. J., & Smith, N. 2011. Nearby supernova rates from the Lick Observatory Supernova Search - II. The observed luminosity functions and fractions of supernovae in a complete sample. *MNRAS*, **412**(Apr.), 1441–1472.
- Maguire, K., Di Carlo, E., Smartt, S. J., Pastorello, A., Tsvetkov, D. Y., Benetti, S., Spiro, S., Arkharov, A. A., Beccari, G., Botticella, M. T., Cappellaro, E., Cristallo, S., Dolci, M., Elias-Rosa, N., Fiaschi, M., Gorshanov, D., Harutyunyan, A., Larionov, V. M., Navasardyan, H., Pietrinferni, A., Raimondo, G., di Rico, G., Valenti, S., Valentini, G., & Zampieri, L. 2010. Optical and near-infrared coverage of SN 2004et: physical parameters and comparison with other Type IIP supernovae. *MNRAS*, **404**(May), 981–1004.
- Marcaide, J. M., Pérez-Torres, M. A., Ros, E., Alberdi, A., Diamond, P. J., Guirado, J. C., Lara, L., Van Dyk, S. D., & Weiler, K. W. 2002. Strongly decelerated expansion of SN 1979C. *A&A*, **384**(Mar.), 408–413.
- McCray, R. 2017. *The Physics of Supernova 1987A*. Page 2181.
- Nakayama, Y., Yata, K., & Aoshima, M. 2017. Support vector machine and its bias correction in high-dimension, low-sample-size settings. *ArXiv e-prints*, Feb.
- Olson, David L., & Delen, Dursun. 2008. *Advanced Data Mining Techniques*. 1st edn. Springer Publishing Company, Incorporated.
- Patat, F., Barbon, R., Cappellaro, E., & Turatto, M. 1994. Light curves of type II supernovae. 2: The analysis. *A&A*, **282**(Feb.), 731–741.
- Peng, J., & Paul, D. 2007. A geometric approach to maximum likelihood estimation of the functional principal components from sparse longitudinal data. *ArXiv e-prints*, Oct.
- Pierel, J. D. R., Rodney, S., Avelino, A., Bianco, F., Filippenko, A. V., Foley, R. J., Friedman, A., Hicken, M., Hounsell, R., Jha, S. W., Kessler, R., Kirshner, R. P., Mandel, K., Narayan, G., Scolnic, D., & Strolger, L. 2018. Extending Supernova Spectral Templates for Next-generation Space Telescope Observations. *PASP*, **130**(11), 114504.
- Ray, A., Petre, R., & Schlegel, E. M. 2001. Chandra and ASCA X-Ray Observations of the Type II-L Supernova SN 1979C in NGC 4321. *AJ*, **122**(Aug.), 966–970.
- Richards, J. W., Homrighausen, D., Freeman, P. E., Schafer, C. M., & Poznanski, D. 2012. Semi-supervised learning for photometric supernova classification. *MNRAS*, **419**(Jan.), 1121–1135.
- Richmond, M. W., Treffers, R. R., Filippenko, A. V., Paik, Y., Leibundgut, B., Schulman, E., & Cox, C. V. 1994. UBVR photometry of SN 1993J in M81: The first 120 days. *AJ*, **107**(Mar.), 1022–1040.
- Rubin, A., & Gal-Yam, A. 2016. Unsupervised Clustering of Type II Supernova Light Curves. *ApJ*, **828**(Sept.), 111.
- Saselli, M., Ishida, E. E. O., Vilalta, R., Agüena, M., Busti, V. C., Camacho, H., Trindade, A. M. M., Gieseke, F., de Souza, R. S., Fantaye, Y. T., & Mazzali, P. A. 2016. Exploring the spectroscopic diversity of Type Ia supernovae with DRACULA: a machine learning approach. *MNRAS*, **461**(Sept.), 2044–2059.
- Savitzky, A., & Golay, M. J. E. 1964. Smoothing and differentiation of data by simplified least squares procedures. *Analytical Chemistry*, **36**, 1627–1639.
- Schlegel, E. M. 1990. A new subclass of Type II supernovae? *MNRAS*, **244**(May), 269–271.
- Shannon, C. E. 2001. A Mathematical Theory of Communication. *SIGMOBILE Mob. Comput. Commun. Rev.*, **5**(1), 3–55.
- Singh, A., Srivastav, S., Kumar, B., Anupama, G. C., & Sahu, D. K. 2018. ASASSN-14dq: a fast-declining Type II-P supernova in a low-luminosity host galaxy. *MNRAS*, **480**(Oct.), 2475–2500.
- Smartt, S. J. 2015. Observational Constraints on the Progenitors of Core-Collapse Supernovae: The Case for Missing High-Mass Stars. *PASA*, **32**(Apr.), e016.
- Smith, N., Chornock, R., Silverman, J. M., Filippenko, A. V., & Foley, R. J. 2010. Spectral Evolution of the Extraordinary Type II_n Supernova 2006gy. *ApJ*, **709**(Feb.), 856–883.
- Sun, F., & Gal-Yam, A. 2017. Quantitative Classification of Type I Supernovae Using Spectroscopic Features at Maximum Brightness. *ArXiv e-prints*, July.
- Taddia, F., *et al.* . 2016. Metallicity from Type II Supernovae from the (i)PTF. *Astron. Astrophys.*, **587**, L7.

- Valenti, S., Sand, D., Stritzinger, M., Howell, D. A., Arcavi, I., McCully, C., Childress, M. J., Hsiao, E. Y., Contreras, C., Morrell, N., Phillips, M. M., Gromadzki, M., Kirshner, R. P., & Marion, G. H. 2015. Supernova 2013by: a Type IIL supernova with a IIP-like light-curve drop. *MNRAS*, **448**(Apr.), 2608–2616.
- Yaron, O., & Gal-Yam, A. 2012. WISeREP—An Interactive Supernova Data Repository. *PASP*, **124**(July), 668.
- Yuan, F., Jerkstrand, A., Valenti, S., Sollerman, J., Seitzzahl, I. R., Pastorello, A., Schulze, S., Chen, T.-W., Childress, M. J., Fraser, M., Fremling, C., Kotak, R., Ruiter, A. J., Schmidt, B. P., Smartt, S. J., Taddia, F., Terreran, G., Tucker, B. E., Barbarino, C., Benetti, S., Elias-Rosa, N., Gal-Yam, A., Howell, D. A., Inserra, C., Kankare, E., Lee, M. Y., Li, K. L., Maguire, K., Margheim, S., Mehner, A., Ochner, P., Sullivan, M., Tomasella, L., & Young, D. R. 2016. 450 d of Type II SN 2013ej in optical and near-infrared. *MNRAS*, **461**(Sept.), 2003–2018.

5. METHODS

The raw spectrum from telescopes will firstly remove the redshift by using the equation $\lambda_{RF} = \lambda_{obs}/(1+z)$, where λ_{RF} is the wavelength in the rest-frame, λ_{obs} the wavelength in the observer frame. Then, a Savitzky-Golay filter is applied to smooth the spectra, which is shown in Fig.8. Considering the black body radiation in the spectra, we adopt an univariate spline method `python.scipy.UnivariateSpline` for continuum removal, instead of fitting the blackbody radiation spectra, because the iron-blanketing effect may cause extra continuum absorption at the wavelength small than 5000 Å (Faran *et al.* 2018). Furthermore, every spectra’ fluxes are re-normalized to average equal zero and variance equal 1. After this step, we have obtained the spectra preserves most informations of their element compositions.

In the whole pre-processing process, we omitted the color and the temperature information in the spectra, but most informations about the element composition (the position and the depth of spectral lines) and the explosion speed (the P-Cygni profile and the pseudo-Equivalent-Width of spectral line) are preserved. Although the classification results are desirable, we will attempt to integrate these information into the model in the future researches.

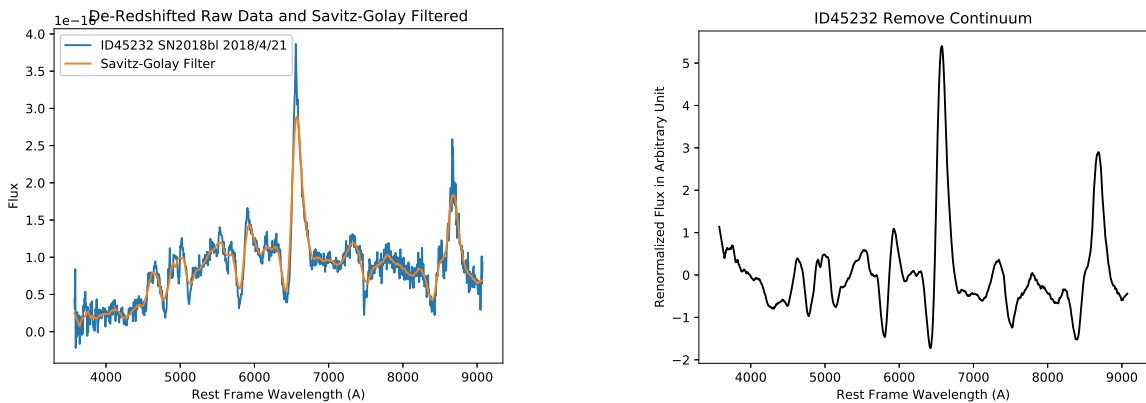


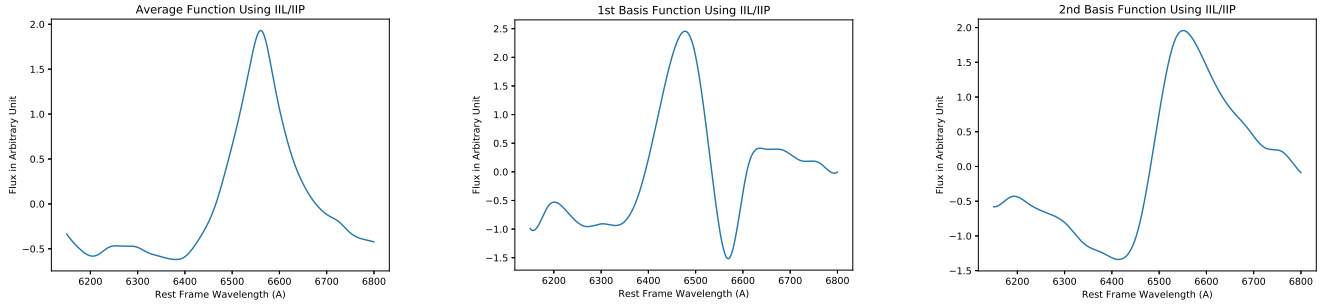
Figure 8. An example spectrum before and after the Savitzky-Golay filter. The window and the order of Savitzky-Golay filter in this plot is $2 \times \text{int}(10/\Delta\lambda) + 1$ and 1, $\Delta\lambda$ is the average wave interval of each spectra. ID45232 is the spectra number in WISEREP.

6. FPCA FIDELITY DISCUSSION

Considering our computer compatibility, we didn’t use all the spectra we downloaded for FPCA analysis. Instead, we randomly choose 15% of them to solve the basis functions. According to some comprehensive research on the Type II SNe (Faran *et al.* 2014b,a) which suggesting the potential continuum between the subtypes of Type II SNe, II/Ib/IIn are also used in FPCA analysis. With these basis functions, the FPCA score of the rest spectra can be calculated from Eq.4. The basis functions of each time may varies, however, we didn’t observe basis functions from different spectra affecting the performance of classifiers or the fidelity when re-constructing the spectra. We also choose only Type IIP and Type IIL spectra for FPCA analysis, the average function and first two basis functions in ‘ H_α ’ window is shown in Fig.6. Comparing to Fig.3, the sharp feature in the first basis function at around 6700 Å is absent, which is probably contributed to the relatively narrow H_α line in Type IIn SNe’ spectra. Nonetheless, with an unknown reason, using these sets of basis functions didn’t increase the performance in classifying Type IIP/IIL SNe.

We choose several pre-processed spectra to compare against the spectra re-constructed by FPCA algorithm, which is shown in Fig.9. For SN2017few’s spectrum here, its FPCA scores are $X(\lambda) \approx \mu(\lambda) - 0.147\phi_1(\lambda) + 0.669\phi_2(\lambda) + 0.087\phi_3(\lambda) \dots$. For SN2013fr’s spectrum here, its FPCA scores are $X(\lambda) \approx \mu(\lambda) - 0.015\phi_1(\lambda) + 0.282\phi_2(\lambda) + 0.024\phi_3(\lambda) \dots$. The re-constructed spectra fits quite well when we choose 40 basis functions, however, some features are lost if we only choose 5 basis functions. Furthermore, we notice that the double-peak feature in SN2017few’s spectrum at 5200-5800 Å has not been reconstructed in the spectrum re-constructed by FPCA scores and basis functions, a close-up look is given in Fig.10.

We choose the last (40th) basis function in ‘Expand’ wave-window. Also, this basis function contains the most (24) peak among other ‘Expand’ basis functions. The average distance between two peaks in the basis function is



approximately 208 \AA , so we suggest that the spectral resolution of ‘Expand’ wavewindow is 208 \AA . In contrast, the distance between the two peaks is approximately 200 \AA , which is similar to the wave resolution of ‘Expand’ wave-window. If the relating spectra contains some extremely sharp features like circumstellar material and the spectra of host galaxy, more basis functions are required to render the spectra. Alternatively, using multiple smaller wave-windows can avoid this problem. In the last (30th) basis function in ‘S’ wave-window, there are 15 peaks and the resolution is 37 \AA , which indicates a better fitting result Fig.11.

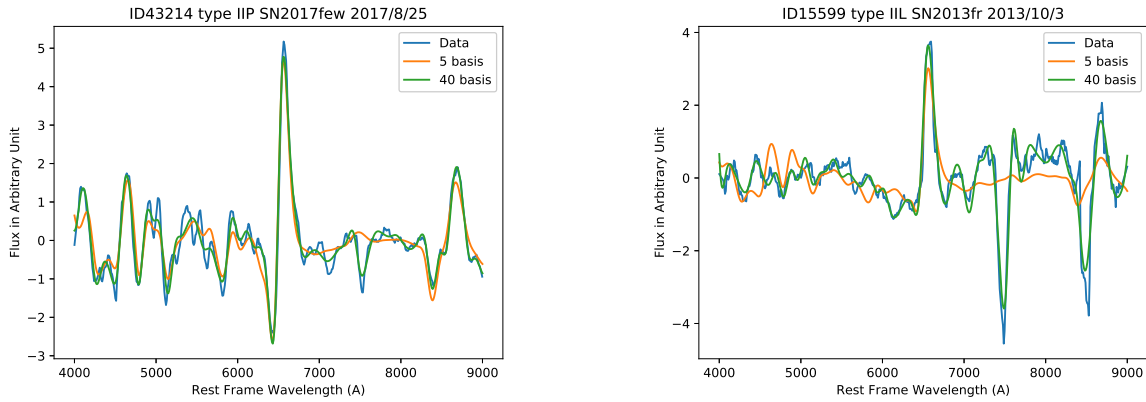


Figure 9. The fitting results of two example spectra, ID number is the spectrum number in WISerEP.

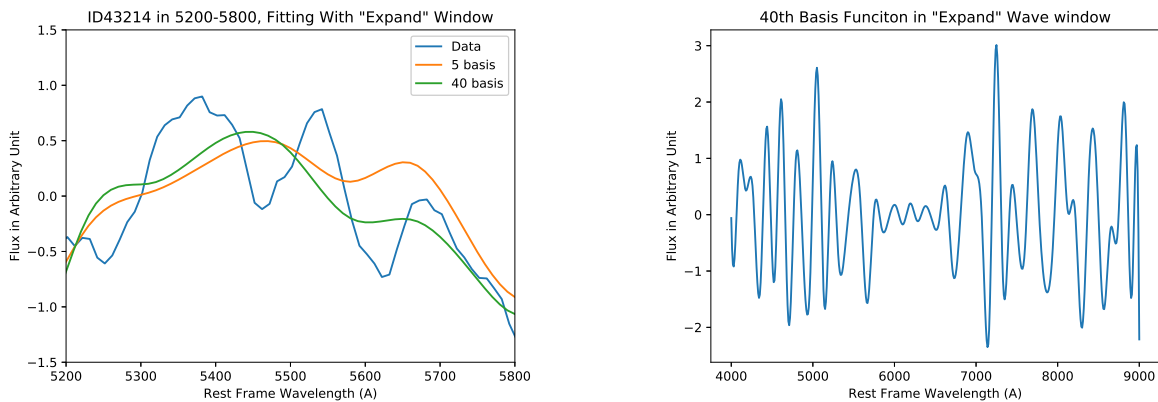


Figure 10. Left: a close-up look of SN2017few spectrum between 5200 and 5800, the fitting result isn’t desirable. The data here are compressed for the FPCA analysis. Right: the 40th basis function in ‘Expand’ wave-window.

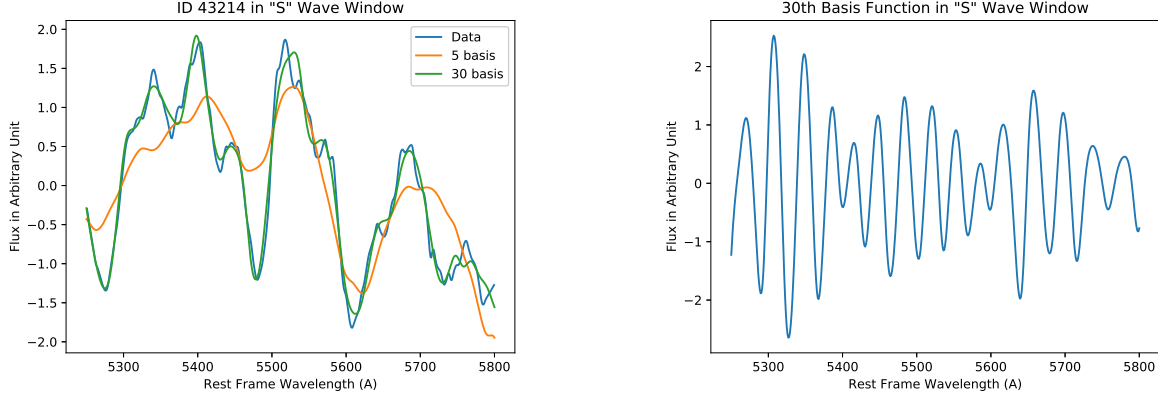


Figure 11. Left: the fitting of SN2017few in ‘S’ wave-window. In this scenario, the fitting fidelity is higher than ‘Expand’ wave-window. To notice, because of the computational capacity, the spectra for FPCA in ‘Expand’ window are down-sampled, which results in the data loss of the peak at 5350. Furthermore, the y-axis scale here differs from Fig.10 because the flux of different wave-windows are re-normalized separately. Right: the 30th basis function in ‘S’ wave-window.

7. DISCUSSION ABOUT THE RELATION OF FPCA SCORES

We plot some figure to illustrate the relation between two FPCA scores of different types of SNe. More plots are uploaded to the website. In Fig.12, we notice Type IIb SNe are close to the lower-left side of the plot, while Type IIc SNe are clustered in the middle-upper side of the plot. For the other types of SNe, it is quite hard to distinguish them. A similar plot concentrated on Type IIP/IIL SNe is shown in Fig.13, the dispersion of Type IIP and IIL SNe are not wholly overlapped, however, it is hard to simply separate them with a curve. Plots using other FPCA scores stumbled upon same problem. We also discussed the evolution of spectra in the FPCA scores’ parametric space, Fig.6 is a paradigm. No conspicuous tendencies are observable in the plot. Because not all the SNe are intensively observed, most SNe are not well-observed in their whole lifetime, so we didn’t take the phase of SNe’ spectra into consideration.

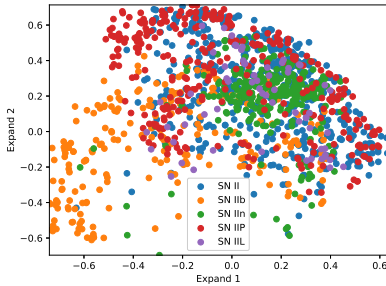


Figure 12. The relation between the first and second FPCA scores in ‘Expand’ wave-window.

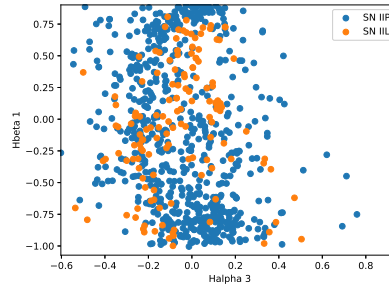


Figure 13. The relation between the ‘ H_{α} ’ and ‘ H_{β} ’ ’s third and first FPCA scores.

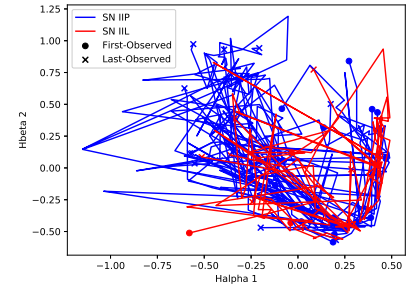


Figure 14. The evolution of Type IIP/IIL spectra, points are linked in the order of observation time.

8. THE PERFORMANCE IN HIGH REDSHIFT SPECTRA

In this paper, no attempt for K-correction(Hogg *et al.* 2002) is done because most Type IIP/IIL objects' redshift are relatively low. However, we analyzed the performance of our classifiers on all 27 objects with redshifts higher than 0.04 (Pierel *et al.* 2018), all of them are Type IIP SNe. We use the cross validation method as is discussed in Section 2.5, then count how many times the spectra is divided in the test set and how many times the spectra are misclassified. Considering the wavelength ranges of these spectra, we only choose ' H_α ' wave window for trial. e

To sum up, the precision of high-redshift spectra in SVM is 0.610, the precision of high-redshift spectra in ANN is 0.627. The classifiers we have trained are not biased, the precision of Type IIP and Type IIL SNe are equal. Comparing to the overall precision of SVM (0.751) and ANN (0.851), we surmise the classifiers' performance are influenced by the redshift.

Table 5. High-z IIP Objects' Performance

Id	Name	Redshift	Fail in SVM	Test in SVM	Fail in ANN	Test in ANN
45175	SN2018aql	0.074	33	95	0	11
44559	SN2018pn	0.048	10	91	0	6
40509	SN2017hk	0.059	89	109	16	18
40495	SN2016ied	0.0479	101	106	6	10
25600	OGLE15xg	0.061	41	90	3	13
21563	OGLE-2015-SN-052	0.06	62	81	13	15
21454	OGLE-2015-SN-009	0.06	3	98	0	7
20707	LSQ14gae	0.041	12	83	2	5
20196	LSQ14eeh	0.09	92	111	1	6
24058	LSQ13cuw	0.25	8	113	0	6
24059	LSQ13cuw	0.25	1	78	2	12
24060	LSQ13cuw	0.25	81	104	5	8
24057	LSQ13cuw	0.25	44	101	5	9
24055	LSQ13cuw	0.25	53	100	2	5
16147	LSQ13cuw	0.25	37	98	4	6
24050	LSQ13cuw	0.25	18	87	6	15
11399	OGLE-2013-SN-011	0.05	40	98	5	6
19426	OGLE-2013-SN-011	0.05	1	105	0	9
8755	CSS120416-131835+213833	0.065	37	84	2	9
8723	LSQ12blb	0.052	95	107	3	12
19049	LSQ12blb	0.052	75	92	6	10
27225	SN2011jj	0.045	1	103	0	13
41519	SN2007tu	0.22	65	94	4	13
41574	SN2007sx	0.1171	1	105	0	15
42123	ESSENCEq060	0.1441	7	86	4	14
42122	ESSENCEq060	0.1441	31	104	9	15
42076	ESSENCEn271	0.241	33	88	3	7
42110	ESSENCEm041	0.22	7	97	0	12
42096	ESSENCEm003	0.219	24	83	7	12
41502	SN2004fj	0.1874	26	94	4	8
41513	SN2004fp	0.2	16	81	2	8
41568	SN2003lg	0.2	15	93	3	6
41380	SN2003kj	0.0784	68	88	6	9

9. TABLE AND DATA

Table 6. SVM performance in single wave-window

Wave-window	C	Precision	Recall	F1-Score	σ_P	σ_R	σ_F
FeMg	3020	0.797	0.796	0.793	0.050	0.050	0.050
H_β	800000	0.796	0.794	0.791	0.040	0.039	0.040
FeOMgSi	3020	0.775	0.774	0.771	0.049	0.049	0.050
S	3020	0.748	0.745	0.740	0.052	0.052	0.053
Na	80000000	0.769	0.766	0.762	0.048	0.047	0.048
H_α	8000000	0.812	0.811	0.809	0.043	0.045	0.045
Gap	800000000	0.732	0.731	0.727	0.043	0.042	0.042
NaMg	3020	0.703	0.700	0.694	0.064	0.063	0.064
Ca	3020	0.793	0.791	0.787	0.059	0.059	0.060
Visible	3020	0.834	0.833	0.830	0.056	0.056	0.057
Expand	3020	0.822	0.820	0.815	0.079	0.079	0.081

Table 7. ANN performance in single wave-window

Wave-window	Nodes in hidden layer	Precision	Recall	F1-Score	σ_P	σ_R	σ_F
FeMg	90	0.810	0.809	0.807	0.051	0.052	0.053
H_β	90	0.826	0.825	0.822	0.048	0.048	0.049
FeOMgSi	90	0.795	0.797	0.793	0.034	0.033	0.034
S	90	0.782	0.780	0.777	0.057	0.055	0.055
Na	40	0.806	0.804	0.799	0.051	0.049	0.051
H_α	90	0.851	0.850	0.849	0.038	0.038	0.038
Gap	40	0.750	0.749	0.747	0.063	0.064	0.064
NaMg	90	0.725	0.721	0.716	0.071	0.068	0.071
Ca	90	0.814	0.812	0.809	0.052	0.051	0.052
Visible	15	0.873	0.871	0.870	0.048	0.049	0.048
Expand	15	0.857	0.858	0.852	0.058	0.060	0.059

Table 8. Performance in Different Dimension FPCA Using ANN and ‘ H_α ’ Wave-Window

Basis Functions	Precision	Recall	F1-Score	σ_P	σ_R	σ_F
30	0.851	0.85	0.849	0.038	0.038	0.038
25	0.847	0.848	0.846	0.043	0.041	0.043
20	0.849	0.85	0.847	0.042	0.045	0.046
15	0.844	0.843	0.841	0.035	0.035	0.034
10	0.842	0.842	0.839	0.028	0.026	0.028
9	0.832	0.833	0.83	0.038	0.036	0.038
8	0.821	0.818	0.816	0.052	0.053	0.054
7	0.769	0.77	0.767	0.055	0.057	0.056
6	0.786	0.784	0.782	0.049	0.05	0.05
5	0.726	0.726	0.723	0.038	0.038	0.038
4	0.696	0.694	0.688	0.045	0.044	0.044
3	0.67	0.67	0.67	0.059	0.057	0.058
2	0.658	0.656	0.65	0.045	0.043	0.045

Table 9. Performance in Different Dimension FPCA Using ANN and ‘Visible’ Wave-Window

Basis Functions	Precision	Recall	F1-Score	σ_P	σ_R	σ_F
50	0.873	0.871	0.87	0.048	0.049	0.048
40	0.854	0.854	0.85	0.038	0.037	0.04
35	0.861	0.859	0.857	0.053	0.051	0.054
30	0.869	0.869	0.864	0.042	0.042	0.042
25	0.873	0.876	0.872	0.049	0.052	0.05
20	0.856	0.854	0.851	0.051	0.056	0.055
15	0.843	0.845	0.841	0.051	0.051	0.052
10	0.85	0.845	0.842	0.079	0.079	0.083
8	0.872	0.873	0.87	0.073	0.073	0.073
7	0.824	0.822	0.819	0.066	0.065	0.064
6	0.775	0.777	0.774	0.05	0.05	0.048
4	0.761	0.763	0.755	0.054	0.055	0.053
2	0.707	0.702	0.7	0.078	0.079	0.079